Modelling the small-scale deposition of snow onto structured Arctic sea ice during a MOSAiC storm using snowBedFoam 1.0.

Océane Hames [1,2,*], Mahdi Jafari [2,*], David Nicholas Wagner [1,2], Ian Raphael [3], David Clemens-Sewall [3], Chris Polashenski [3,4], Matthew D. Shupe [5,6], Martin Schneebeli [1], and Michael Lehning [1,2]

[1]WSL Institute for Snow and Avalanche Research SLF, Davos, Switzerland
[2]CRYOS, School of Architecture, Civil and Environmental Engineering, EPFL, Lausanne, Switzerland
[3]Thayer School of Engineering, Dartmouth College, Hanover, New Hampshire, USA
[4]USACE-CRREL Alaska Projects Office, Fairbanks, Alaska, USA
[5]NOAA Physical Science Laboratory, Boulder, Colorado, USA
[6]Cooperative Institute for the Research in Environmental Sciences, University of Colorado Boulder, Boulder, Colorado, USA
[*]These authors contributed equally to this work.

Correspondence: Océane Hames (hames.oceane@gmail.com)

Abstract. The remoteness and extreme conditions of the Arctic make it a very difficult environment to investigate. In these regions, the wind has a substantial effect and redistributes a large part of the snow, which complicates precipitation estimates. Moreover, the snow mass balance in the sea ice system is still poorly understood, notably due to the complex structure of its surface. Quantitatively assessing the snow distribution on sea ice and its connection to the sea ice surface features is an important step to remove these uncertainties. In this work we introduce *snowBedFoam 1.0.*, a physics-based snow transport model implemented in the open source fluid dynamics software OpenFOAM. We combine the numerical simulations with terrestrial lidar observations of surface dynamics to simulate snow deposition on a piece of MOSAiC sea ice with a complicated structure typical for pressure ridges. The results demonstrate that a large fraction of snow accumulates in their vicinity, which compares favorably against terrestrial laser scans. However, the approximations imposed by the numerical framework together with potential measurement errors (precipitation) give rise to quantitative inaccuracies. The modelling of snow distribution on sea ice should help to better constrain precipitation estimates and more generally assess and predict snow and ice dynamics in the Arctic.

1 Introduction

Sea ice figures prominently in a broad range of environmental, socioeconomic and geopolitical applications (Matthews et al., 2019; Yumashev et al., 2017; Huntington et al., 2016). In the past years, the interest in sea ice has grown substantially as it seems to respond very sensitively to climate change: from the late 1970s until the present, the monthly average of the Arctic sea ice extent has undergone an important reduction, with a downward trend of 13.1% per decade relative to the 1981-2010 average (Perovich et al., 2020). Being able to predict the future evolution of this environment implies having a sufficient knowledge of the mechanisms underlying the ice generation and destruction dynamics.

20   Recently, different authors have stressed the need to have a robust quantification of the snow distribution since it seems to play a significant role in both the melt and growth of sea ice (Leonard and Maksym, 2011; Webster et al., 2018): the insulating capacities of snow as well as its high albedo can profoundly impact the internal energy budget of sea ice (Trujillo et al., 2016). Snow furthermore modifies the topography and the aerodynamic roughness of the sea ice surface, which impacts the turbulent energy transfer with the atmosphere (Andreas and Claffey, 1995). Lastly, snow can contribute to the ice mass as its weight

25   reduces the freeboard, which may result in snow-ice formation (Ackley et al., 1990; Sturm and Massom, 2016); the importance of this process is expected to grow in the future with the thinning of the Arctic ice (Maslanik et al., 2007; Provost et al., 2017) and increasing precipitation (Bintanja et al., 2020).

       Hence, snow is presented as an integral component of the ocean - sea ice - snow - atmosphere system and quantifying its distribution is a key to a better understanding of the sea ice mass balance. Also, Arctic precipitation estimates could be signifi-

30   cantly improved by an accurate assessment of the snow deposition on sea ice. The strong winds encountered in this environment lead to large uncertainties in both measurements and model projections of precipitation (Boisvert et al., 2018). Measuring snow deposition and connecting the snow mass balance to snowfall is a way to better constrain the current precipitation estimates and improve meteorological models.

       Despite its importance, the current knowledge on sea ice snow depth distribution and its spatio-temporal evolution is limited

35   due to sparse observational evidence (Sturm and Massom, 2016; Liston et al., 2018). The amount of snow that gets accumulated, redistributed, sublimated and transported to the open water is determined by the complex interaction between snowfall, wind, and the presence and spacing of open leads; the influence of each of these processes, however, remains uncertain (Déry and Tremblay, 2004). In particular, surface features such as pressure ridges have a substantial effect on the snow distribution: by serving as aerodynamic obstacles, they enhance the deposition of drifting and blowing snow, which leads to the formation of

40   depositional features such as drift aprons (Trujillo et al., 2016; Liston et al., 2018; Sommer et al., 2018). However, detailed quantitative spatial representations of the effect of such topographical structures are limited.

       Several authors have investigated the snow distribution on sea ice in the recent years. Spatial measurements over a small-scale area of Antarctic sea ice ($\sim$100$\times$100 m) with terrestrial laser scanning by Trujillo et al. (2016) were used to characterize the influence of a storm on snow distribution patterns and their relation to the surface topography. Snow drifts were found to

45   form mostly behind the topographical obstacles, elongated along the dominant wind direction. To our knowledge, such spatial observations of snow deposition are non-existent in the literature for Arctic sea ice.

       From a numerical perspective, Liston et al. (2018) recently applied a snow-evolution modelling system (SnowModel, Liston and Elder (2006)) to simulate snowdrifts and snow-depth distributions around sea ice pressure ridges. The authors ran a one-year simulation over an Arctic sea ice domain (1.5km $\times$ 1.5km) containing a ridged topography, which they tested against

50   measurements. Results showed strong snow deposition behind the pressure ridges and snow-free sea ice at their top, with partial accumulation along the upwind side of the ridges. The employed topographical data was based on radar-derived images of ice as more precise spatial observations were not available. The study suggested that improvement could be made through the use of surface based and airborne light detection and ranging (lidar), which we perform in this study.

Generally speaking, spatial variability of snow deposition around complex terrain (e.g. sea ice) is not yet fully understood
(Grünewald et al., 2010) and multiple model approaches exist that try to describe it (Liston et al., 2007; Mott and Lehning, 2010; Wang and Huang, 2017). In particular, the modeling framework developed by Comola et al. (2019) combines large eddy simulation (LES) for the flow and a Lagrangian stochastic model (LSM) for snow particle trajectories. Their model simulations demonstrate that different deposition patterns can emerge from different combinations of scale- and velocity-dependent dimensionless parameters. Thus, various factors influence the spatial variability of snow distribution on sea ice and numerical modeling can help with understanding dominant processes.

Herein we present *snowBedFoam 1.0.*, a new Eulerian-Lagrangian snow transport solver implemented in the computational fluid dynamics (CFD) software OpenFOAM (OpenCFD Ltd, 2019) that we employ to simulate the snow distribution patterns on a piece of sea ice containing some pressure ridges. Several data sets from the recent MOSAiC (Multidisciplinary Drifting Observatory for the Study of Arctic Climate) expedition (Alfred-Wegener-Institut Helmholtz-Zentrum für Polar- und Meeresforschung (AWI), 2020) are used for this purpose. The first one is terrestrial laser scan (TLS) data that we employ as a topographical base for the numerical domain in the simulations. We secondly use meteorological measurements from MOSAiC to set-up the wind and precipitation settings in the model and simulate specific atmospheric events. Finally, we compare the simulation output to real snow distribution measurements obtained by differencing successive digital elevation models (DEMs) of the snow surface. The TLS technology permits the survey of snow depth variability in a very high resolution (Prokop et al., 2008) and is particularly well suited for studying snow transport processes at small scales.

The novelties of the numerical approach developed in this study are multiple. First, to our knowledge, the OpenFOAM software has never been employed for the modelling of aeolian snow transport with such a detailed representation of the snow particle-bed interactions. Second, we initiate the use of the physical model of snow transport based on CFD and LSM (Sharma et al., 2018; Comola et al., 2019) for sea ice applications, in addition to the integration of real snowfall and wind data as forcing parameters. Finally, the use of TLS elevation data as a base for the sea ice surface in the simulation domain has not achieved yet in the literature (Liston et al., 2018). The present work is a first step towards the accurate modelling of snow distribution on sea ice and could contribute in a larger frame to the improvement of precipitation and sea ice mass balance estimates in model projections.

This article begins with the presentation of the MOSAiC measurements that were employed to produce the results in the subsequent parts. In a second stage, we describe the OpenFOAM snow transport model and the associated equations that were implemented to reproduce the snow erosion and deposition processes on sea ice. Then, we present the details related to the simulations, including the modelling assumptions and the numerical settings such as the forcing parameters. In the last section, the results from the simulations are analyzed and compared to real DEM measurements. Discussion and concluding remarks follow.

2 Data and Methods

85

Several processing steps were required to generate the results presented in this work. In this section we successively describe: (1) the MOSAiC measurement campaign conducted on Arctic sea ice and the related data sets employed here; (2) the implementation of the snow transport model in the OpenFOAM software; (3) the assumptions and general settings of the simulations aiming to reproduce the snow distribution on sea ice.

2.1 MOSAiC Campaign

90

Detailed observations of snow surface topography were conducted during the MOSAiC expedition which took place in the Central Arctic from September 2019 to October 2020 (Alfred-Wegener-Institut Helmholtz-Zentrum für Polar- und Meeresforschung (AWI), 2020). Trapped in the Arctic ice for a nearly full annual cycle, the research vessel Polarstern (Alfred-Wegener-Institut Helmholtz-Zentrum für Polar- und Meeresforschung (AWI), 2017) served as the center for data collection on

95 a drifting sea ice floe: a kilometer-wide network of monitoring stations was set up in its surroundings, allowing various and extensive measurements.

This study focuses on repeated laser scans of snow on second-year sea ice that were successively operated on November 6 and November 13, 2019 (Clemens-Sewall, 2021). The scanned region after processing covers a total area of 390 m x 340 m and its location relative to the MOSAiC sea ice floe is shown in Figure 1 (black frame). A Riegl VZ-1000 scanner (RIEGL,

100 2017) was positioned at several locations with sufficient scan overlap to generate a three-dimensional (3D) cloud of points over the zone of interest. The emitter of the scanner was placed as high as possible to avoid shadowing issues and the scan positions were recorded relatively to an intrinsic project coordinate system. Details about the use of TLS for sea ice measurements can be found in Polashenski et al. (2012). Before its use, the raw point cloud was post-processed with the RiSCAN PRO v2.10. (RIEGL, 2020) software and interpolated with QGIS (QGIS, 2020). Several corrections were made which included filtering,

105 removal of outliers / non-static objects and the shift and rotation of tie points. As a last step, the point clouds were aggregated at grid scales between 20 cm to 1 m and interpolated into digital snow surfaces (Prokop et al., 2008). We chose to use the highest resolution available to fully capture the small-scale structure of the surface. The two final DEMs reveal the surface position of the snow at two distinct times and their difference yields snow accumulation patterns that could be compared to the numerical results generated with snowBedFoam 1.0. Change in snow-depth values were converted to comparative units of

110 areal mass by multiplication with a constant snow density value of 210 kg.m^{-3} measured simultaneously during the campaign. This approach fails to take into account the spatial variability of snow density that is expected over the sea ice floe, especially in the vicinity of topographical features. MOSAiC research into this topic is currently ongoing and we expect some influence on the quantitative results presented in this paper.

Besides the sea ice surface topography, wind data was also required to accurately represent the mean flow field conditions

115 in the numerical simulations. Wind information was collected using a meteorological station that was permanently installed on the investigated ice floe as part of the MOSAiC measuring network (Met City, green dot mark in Figure 1). The meteorological station included three 3D Metek uSonic-3 Cage MP anemometers and three Vaisala HMT temperature and humidity sensors
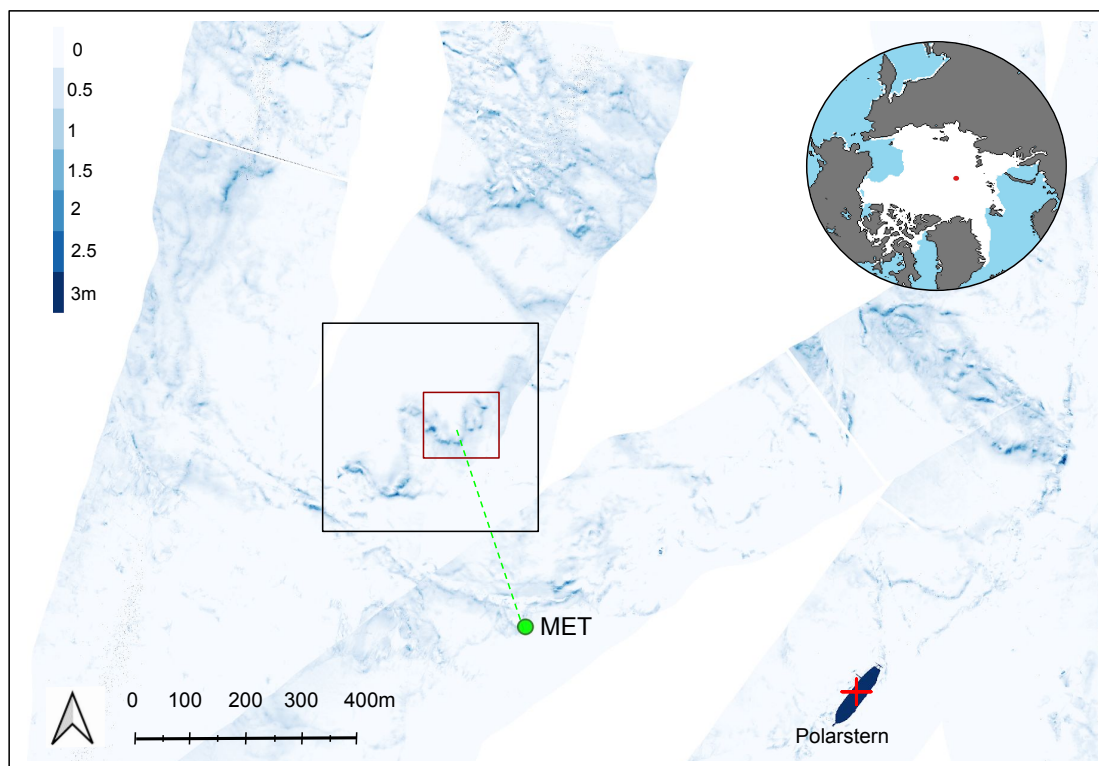
Figure 1. Aerial laser scan (ALS) of the sea ice floe taken on November 12, 2019 during a helicopter flight. The black rectangle pinpoints the zone covered by the terrestrial laser scans (TLS) which were used in the simulations. More particularly, the sea ice area framed within the red rectangle served as a base for the snowBedFoam 1.0. computational domain. The green dot mark highlights the position of the MOSAiC meteorological station where wind measurements were taken. The red cross points out the position of the Polarstern ice-breaker (Alfred-Wegener-Institut Helmholtz-Zentrum für Polar- und Meeresforschung (AWI), 2017). The map on the top right corner shows the position of Polarstern on the day of the ALS measurement.

located at nominal 2 m, 6 m and 10 m heights. In particular, hourly data for wind direction and friction velocity were used to set up the flow parameters in our snow transport model. The MOSAiC atmosphere surface energy flux team performed
120 the post-processing of the measurements, which included sonic data treatment (friction velocity) and correction of orientation (wind direction).

At last, precipitation estimates during MOSAiC were recorded, among other instruments, using ship-based Ka-Band ARM (Atmospheric Radiation Measurement) Zenith Radar (KAZR) reflectivities (Atmospheric Radiation Measurement (ARM) user facility, 2019) at a 280m range gate along with a reflectivity-based retrieval (Matrosov, 2007). Our steps proceed in the same
125 way as Wagner et al. (2021), whose analysis suggests that this data is on the whole reliable, despite a tendency towards overestimation. The radar recorded a 7-hour long snowfall event during the inter-TLS period (on November 11, 2019), which was included in OpenFOAM by releasing particles in the domain at the average measured rate.

2.2 snowBedFoam 1.0. : an OpenFOAM snow transport model

2.2.1 Eulerian-Lagrangian solver

130 This section describes the three-dimensional Eulerian-Lagrangian model we developed in the open source platform Open-FOAM (Open Field Operation and Manipulation) (OpenCFD Ltd, 2019) to simulate snow transport. OpenFOAM is a C++ object-oriented toolbox used to develop numerical solvers providing a solution to continuum mechanics problems (Weller et al., 1998), which is based on the finite volume method (FVM) for fluid dynamics computations. A comprehensive review of this field of research is beyond the scope of this paper; further details on the implementation of the FVM in the software and

135 on the various techniques developed over the years can be found in works such as Moukalled et al. (2015).

The so-called *DPMFoam* solver originally implemented in OpenFOAM version 2.3.0. was adapted to simulate the aeolian transport of snow particles. This multiphase flow solver handles coupled Eulerian-Lagrangian phases, which involves a finite number of particles spread in a continuous phase (OpenFOAM API Guide, 2006a). It is based on the Lagrangian particle tracking (LPT) technique called discrete particle method (DPM), which models the system at the micro-mechanical level and

140 tracks the motions of all the particles, or agglomerates of particles (parcels) (Cleary and Prakash, 2004). LPT modelling is the most straightforward and effective approach to obtain the deposition and erosion locations of snow (Wang and Huang, 2017). In DPMFoam, the Eulerian continuum equations including particle volume fraction are solved for the fluid phase whereas Newton's equations for motion are solved to determine the trajectories of the particles (parcels). Fernandes et al. (2018) tested the solver against various data types and found a good agreement with results from the literature. The governing equations for

145 particle and fluid-phase systems employed in DPMFoam are described hereafter.

Governing equations for the particle system

A particle in movement may exchange momentum and energy with other particles, walls or with the surrounding fluid (Fernandes et al., 2018). Most of the typical forces acting on a particle in a granular flow can be included within snowBedFoam 1.0., if required. We chose to adopt a two-way coupling method for our sea ice simulations considering reciprocal action between fluid

150 and particles, while other interactions (e.g. particle - particle) were neglected. In this study, the snow particles were assumed to be subject to gravity and atmospheric drag, and the governing equation for particle motion can be expressed through Newton's second law :

$$m_i \frac{d\boldsymbol{U}_i^p}{dt} = m_i \boldsymbol{g} + \boldsymbol{F}_d \tag{1}$$

where $\boldsymbol{U}_i^p$ is the particle velocity, $\boldsymbol{F}_d$ is the drag force, $\boldsymbol{g}$ the gravity acceleration vector and m_i is the mass of a spherical

155 particle. The latter is formulated as $m_i = \frac{1}{6}\pi\rho_p d_i^3$, with d_i the diameter and ρ_p the density of the particle. The drag force stems from the particle–fluid interaction and is proportional to the relative velocity between the phases. Numerous drag models are available in the OpenFOAM framework: we chose to adopt the commonly used sphere-drag model based on the assumption of solid spheres (OpenFOAM API Guide, 2006c). If $\boldsymbol{U}^f$ represents the fluid velocity, then the corresponding drag force exerted

on a spherical particle is defined as

$$160 \quad \boldsymbol{F}_d = \frac{3 m_i C_D Re_p \mu}{4 \rho_p d_i^2} (\boldsymbol{U}^f - \boldsymbol{U}_i^p) \tag{2}$$

where μ represents the dynamic viscosity and Re_p is the particle Reynolds number

$$Re_p = \frac{d_i |\boldsymbol{U}^f - \boldsymbol{U}_i^p|}{\nu} \tag{3}$$

characterizing the relative importance between the inertial and viscous forces acting on a particle, with ν the kinematic viscosity. C_D is the so-called drag coefficient and is defined as follows

$$165 \quad C_D = \begin{cases} 0.424 & \text{for } Re_p > 1000 \\ \frac{24}{Re_p} \left(1 + \frac{1}{6} Re_p^{2/3} \right) & \text{for } Re_p \leq 1000 \end{cases} \tag{4}$$

Information about the forces and coupling modes available for particle modelling in OpenFOAM can be found in OpenCFD Ltd (2018) and OpenFOAM API Guide (2006b).

Governing equations for the fluid-phase system

The flow equations implemented in DPMFoam involve the fluid-phase volume fraction ϵ_f in an Eulerian cell expressed as:

$$170 \quad \epsilon_f = \max \left(1 - \frac{1}{V_{cell}} \sum_{i=1}^{N_p} f_i^p V_i \ , \ \epsilon_{fmin} \right) \tag{5}$$

with V_{cell} the cell volume, f_i^p the fractional volume of a particle i located in the cell under consideration, V_i the volume of particle i and ϵ_{fmin} a very small value which limits the cell from being fully occupied by a particle. N_p represents the total number of particles present in the computational cell. The Navier-Stokes equations (Eq.6) and the volume-averaged continuity equation (Eq.7) are solved for an incompressible fluid phase in the presence of a secondary particulate phase:

$$175 \quad \frac{\partial (\epsilon_f \boldsymbol{U}^f)}{\partial t} + \nabla \cdot (\epsilon_f \boldsymbol{U}^f \boldsymbol{U}^f) = \mathscr{P} - \nabla P + \nabla \cdot (\epsilon_f \boldsymbol{\tau}_f) - \boldsymbol{F}_p + \epsilon_f \mathbf{g}, \tag{6}$$

$$\frac{\partial \epsilon_f}{\partial t} + \nabla \cdot (\epsilon_f \boldsymbol{U}^f) = 0 \tag{7}$$

where P is the modified pressure (p/ρ_f, with ρ_f being the fluid density) and $\boldsymbol{\tau}_f$ is the fluid-phase viscous stress tensor. $\mathscr{P}$ represents the imposed large-scale driving force in the streamwise direction which was added within the core code of the solver.
180 It is described as:

$$\mathscr{P} = -\frac{1}{\rho_f} \frac{\partial \widetilde{p_\infty}}{\partial x} = \frac{u_*^2}{L_z} \tag{8}$$

with L_z the vertical extent of the numerical domain and u_* the surface friction velocity. The sink term $\boldsymbol{F}_p$ in the momentum equation (Eq.6) accounts for the two-way coupling between the fluid-phase and the particles. As the fluid drag acting on each particle is known, this term is computed as a volumetric fluid–particle interaction force given by:

$$\boldsymbol{F}_p = \frac{\sum_{i=1}^{N_p} \boldsymbol{F}_{d,i}}{\rho_f V_{cell}} \tag{9}$$

where $\boldsymbol{F}_{d,i}$ is the drag force exerted on particle i. $\boldsymbol{F}_p$ is here presented in a discretized form.

2.2.2 Snow-wind interaction model

The aeolian transport of solid particles can be classified into three modes (Bagnold, 1941), namely: 1) *creeping*, which consists of the rolling of particles along the surface; 2) *saltation*, which occurs when particles follow ballistic trajectories and involves mechanisms such as aerodynamic lift along with rebound and entrainment (splash) of snow grains; 3) *suspension*, which entails the same mechanisms as saltation but applies to smaller grains transported at higher elevations and over larger distances. We developed several utilities within the OpenFOAM Lagrangian library to introduce the processes of aerodynamic lift, rebound and splash of particles. Thus, our new modelling tool simulates the redistribution of snow through saltation and suspension.

The governing equations that were implemented in the solver stem from snow transport-related publications from various authors (Anderson and Haff, 1991; Comola and Lehning, 2017; Bagnold, 1941). We employed a similar set of equations for particle-flow interaction to the one implemented in the large eddy simulation - Lagrangian stochastic model (LES-LSM) which was used to generate publications such as the ones of Comola et al. (2019) and Sharma et al. (2018). The equations relevant for our snow transport model are summarized subsequently.

Aerodynamic entrainment

Grains lying on the snowbed can be entrained into the near-surface layer of the atmosphere when the fluid surface shear stress $\tau_{f,surf}$ is large enough to lift them up, namely when it exceeds a threshold value defined as (Bagnold, 1941)

$$\tau_{th} = A^2 g \langle d_p \rangle (\rho_p - \rho_f) \tag{10}$$

where $\langle d_p \rangle$ is the mean particle diameter and A is an empirical constant. In each grid cell, the number of particles aerodynamically entrained by the fluid at each timestep, N_{ae}, linearly increases with the excess shear stress according to the formulation of Anderson and Haff (1991):

$$N_{ae} = \frac{C_e}{8\pi \langle d_p \rangle^2} (\tau_{f,surf} - \tau_{th}) \Delta x \Delta y \Delta t \tag{11}$$

where C_e is an empirical parameter set to 1.5 (Doorschot and Lehning, 2002), Δx and Δy are the grid dimensions in the streamwise/spanwise directions and Δt is the simulation timestep. Once N_{ae} is determined, properties such as the particle diameter, initial velocity magnitude and ejection angle are sampled from statistical distributions according to Clifton and Lehning (2008). More details can be found in their work.

Rebound and splash entrainment

Depending on its path, a snow particle present in the fluid might hit the surface upon which it can not only rebound -defined as *rebound* entrainment- but also eject other particles from the bed to the overlying fluid, defined as *splash* entrainment. The probability P_r that the snow particle rebounds when impacting the bed is given by Anderson and Haff (1991) as follows

$$P_r = P_m(1 - e^{-\gamma v_i}) \tag{12}$$

where P_m is the maximum probability equal to 0.9 for snow (Groot Zwaaftink et al., 2013), γ is an empirical constant equal to 2, and v_i is the velocity magnitude of the impacting particle. When rebounding, the particle is assumed to have a velocity magnitude of $v_r = 0.5v_i$ (Doorschot and Lehning, 2002) and the rebound angle is determined from a statistical distribution according to Kok and Rennó (2009).

Concerning the splash entrainment, the number of particles ejected from the bed N_{splash} is defined as the minimum between N_E and N_M whose expressions are (Comola and Lehning, 2017):

$$N_E = \frac{(1 - P_r\epsilon_r - \epsilon_{fr})d_i^3 v_i^2}{2\langle v\rangle^2(\langle d\rangle + \frac{\sigma_d^2}{\langle d\rangle})^3 \left(1 + r_E\sqrt{5[1 + (\frac{\sigma_d}{\langle d\rangle})^2]^9 - 5}\right) + 2\frac{\phi}{\rho_p}} \tag{13}$$

$$N_M = \frac{(1 - P_r\mu_r - \mu_{fr})d_i^3 v_i cos\alpha_i}{\langle v\rangle^2(\langle d\rangle + \frac{\sigma_d^2}{\langle d\rangle})^3 \left(\langle cos\alpha\rangle\langle cos\beta\rangle r_M\sqrt{[1 + (\frac{\sigma_d}{\langle d\rangle})^2]^9 - 1}\right)} \tag{14}$$

N_M and N_E are the number of ejections predicted by the momentum and energy balance, respectively. In Eq.(13), ϵ_{fr} and ϵ_r are the fractions of impact energy lost to the bed and kept by the rebounding particle, respectively. μ_{fr} and μ_r are their equivalent for momentum in Eq.(14). $\langle d\rangle$ and σ_d are the mean and standard deviation of ejecta's diameter, $\langle v\rangle$ its mean velocity and α and β the horizontal and vertical ejection angles. ϕ is the cohesive bond exerted on a particle by its neighboring particles. r_M and r_E are correlation coefficients linking mass and velocity. More details about the derivation of these formulations can be found in the work of Comola and Lehning (2017). Similarly to the aerodynamic entrainment, the characteristics of the splashed particles are randomly sampled from statistical distributions. Overall, details about the equations of the snow surface-flow interaction can be found in the Supplementary Material of the study by Sharma et al. (2018).

2.3 Simulation Settings

2.3.1 Numerical Domain

The mesh employed for the OpenFOAM simulations on sea ice was generated based on the first set of TLS scans dating from November 6, 2019. The red-framed area in Figure 1 pinpoints the part of the ice surface scanned with ground-based lidar that was used as a base for the numerical domain ($\sim$110 m$\times$120 m). This zone was selected due to its central position in the DEM

along with the variation in height, shape and orientation of its ridged ice. A 10 m wide buffer zone was created between the area of interest and the lateral boundaries to limit the influence of the latter on the simulated flow. The vertical extent of the domain

240 was set to 15 m, with a maximum pressure ridge height of 3.1 m. We chose to limit the dimensions of the numerical domain to perform less computationally intensive simulations. However, the snowBedFoam 1.0. solver could be run on larger-scale areas if required.

The numerical domain with gridded sea ice-topography was generated with STereo Lithography (STL) input data. Linear grid stretching was applied in the vertical direction to insure sufficient grid points in the saltation region while limiting the

245 computational costs in the upper part of the domain; the vertical grid spacing dz ranges between $dz = 0.5$ m for the coarsest grid resolution and $dz = 0.1$ m for the finest grid resolution near the surface. In the streamwise and cross-stream directions, a uniform grid was applied with an average resolution dx , $dy = (0.5$ m). The final mesh is composed of 2 million hexahedral cells.

2.3.2 Boundary conditions

250 The set of simulations in this work were ran by imposing periodic boundary conditions (PBCs) at the lateral sides of the domain (Fig. 2). PBCs are based on the inter-connection of the mesh elements on opposite faces: OpenFOAM treats the flow at a periodic boundary as if the opposing periodic plane was a direct neighbor to the cells adjacent to the first periodic boundary. This has the advantage to keep a reasonable domain size while guaranteeing fully developed velocity profiles within the domain. For Lagrangian applications, PBCs imply that a particle reaching a lateral boundary is directly re-injected in the

255 domain through the corresponding cell of the connected periodic plane. Regarding the sea ice surface boundary, no-slip and impermeability boundary conditions were imposed at the wall for the horizontal and vertical velocity components, respectively. At the top boundary the horizontal components of velocity were set to Neumann zero-gradient BCs and the vertical component was set to a null value.

2.3.3 Numerics

260 The Reynolds-Averaged Navier-Stokes (RANS) method and $k - \epsilon$ closure model were employed to solve the set of equations for a neutral flow. We refer to the introductory paper by Launder and Spalding (1974) and to flow dynamics reference books (e.g. Stull (1988)) for additional details on these particular CFD techniques. To discretize the equations, the Gauss linear and bounded Gauss upwind schemes, respectively, were used for the terms with gradient and divergence operations while the Euler scheme was chosen for the discretization of the transient terms (Moukalled et al., 2015). To assure a faster numerical

265 convergence and minimize the computational effort, the model was initialized with a standard logarithmic wind profile within the boundary layer.

It should be mentioned that the particle mass balance was checked for each of the implemented submodels (including the injection model for precipitation). Moreover, a validation study against the well-established LES-LSM was conducted after the implementation of the new snowBedFoam 1.0. model (not shown here). The results for wind-field and particle mass flux were
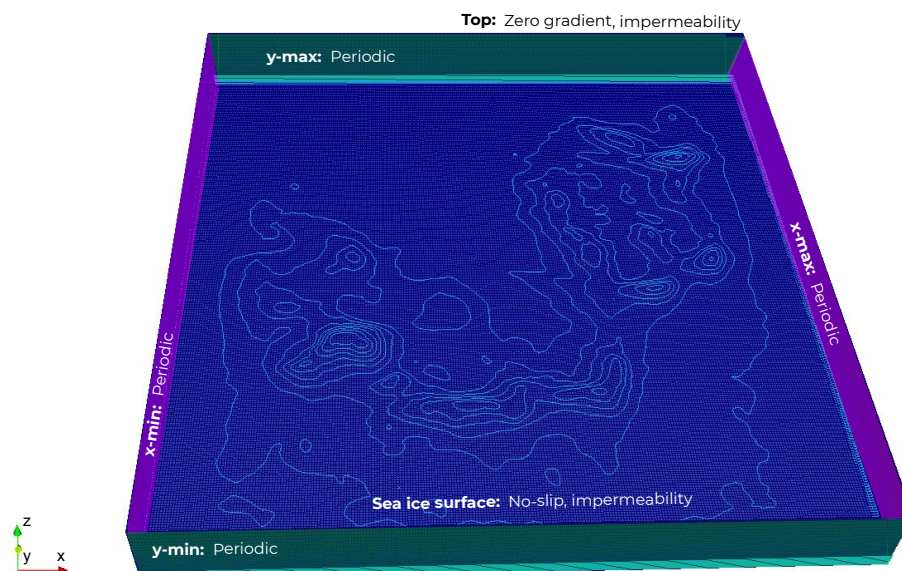
Figure 2. Boundary conditions applied at the six domain patches in the OpenFOAM snow transport simulations. Similar colours are used to represent the corresponding periodic patches.

in good agreement despite fairly distinct grid structure and boundary conditions. This has further strengthened our confidence in the validity of the OpenFOAM model.

2.3.4 Particle and Flow Properties

The flow properties were set in the simulations to approximate as much as possible the mean field conditions for the period between the two MOSAiC scans of interest. For this purpose, the meteorological time series were decomposed into four distinct periods for which the wind speed and direction were averaged (colored areas I-IV in Figure 3), following a successful strategy introduced by Mott and Lehning (2010). These specific intervals were selected based on the friction velocity and duration: any time period with a minimum span of 3 hours and a friction velocity higher than $0.2 \, \mathrm{m.s^{-1}}$ was considered as having a substantial influence on the snow deposition patterns. The friction velocity threshold was chosen based on the publications from various authors who found that snow transport was initiated above this value (He and Ohara, 2017; Clifton et al., 2006; Doorschot et al., 2004). The model was initialized with wind fields characteristic for the respective events to reproduce as accurately as possible the measured snow distribution. Regarding precipitation, the MOSAiC meteorological instruments recorded a 7-hour long snowfall on November 11 (Figure 3, event IV) which we reproduced in the model.

A total of four simulations mimicking the selected time periods were ran with OpenFOAM, whose forcing parameters and time spans are summarized in Table 1. Symbols I to IV in the first column connect with the characters displayed at the top of Figure 3. In the last two columns the values for friction velocity and wind direction correspond to the averages over each event.

Table 1. Snow transport and precipitation events identified during the period between the successive laser scans (2019).

Event	Start Time	End Time	Friction Velocity	Wind Direction
–	dd.mm HH:MM	dd.mm HH:MM	m.s^{-1}	°
I	06.11 12:00	06.11 23:00	0.27	86
II	08.11 21:00	09.11 06:00	0.24	320
III	10.11 23:00	11.11 11:00	0.29	182
	11.11 18:00	13.11 06:00		
IV	11.11 11:00	11.11 18:00	0.45	180

In order to limit the computational effort, the total mass deposition values were extrapolated to the duration of the measured wind events using the particle deposition rates after 1000 s of simulation, which represents an approximation to a steady state situation.

In this context, we verified that the cell deposition rates and distribution patterns do not show strong trends for longer runs.
290 Once a simulation time of 1000s was reached, the particles aloft in the air got progressively deposited through the deactivation of the fluid driving force in snowBedFoam. This strategy allows to mimic the preferential deposition subsequent to a snow transport event, once that the wind shear stress is too weak to keep snow in the air. The four final snow-mass distribution results were superimposed to approximate as closely as possible the real snow-depth changes measured with the TLS.

The snow properties in the simulations (Table 2) were selected on the basis of previous values reported in the literature. All
295 particles were assumed to be spherically shaped and constituted of pure ice. From a dimensional point of view, the mean grain size is as defined in Comola and Lehning (2017) in their snow splash entrainment model; it is also in line with the findings of Nemoto and Nishimura (2004) and Gromke et al. (2014) who measured dimensions of transported snow grains. The particle size distribution of snowflakes is approximated using the log-normal law, although this parameter proved not to affect the deposition patterns (Wang and Huang, 2017). For simulation IV in particular, the average precipitation rate was set according
300 to KAZR snowfall retrievals (280m range gate) from the detected storm event (Wagner et al., 2021).

The last two parameters relate to the surface interaction equations of the model. A is a constant used in the shear stress threshold formulation (Bagnold, 1941), which we set equal to 0.2 for snow based on wind-tunnel experiments (Clifton et al., 2006). The bed cohesion parameter ϕ involved in the ejection entrainment (Comola and Lehning, 2017) represents the mean bounding energy between the grains of the snowbed and is usually found in the range $10^{-10}-10^{-8}$ J (Gauer, 2001). A sensitiv-
305 ity analysis showed that this parameter does not substantially influence the results for the range of friction velocities employed in this work; therefore, an intermediate value (10^{-9} J) in the above-mentioned range was selected. All the simulations were initiated without particles for the first 100 s to ensure a fully developed flow-field.
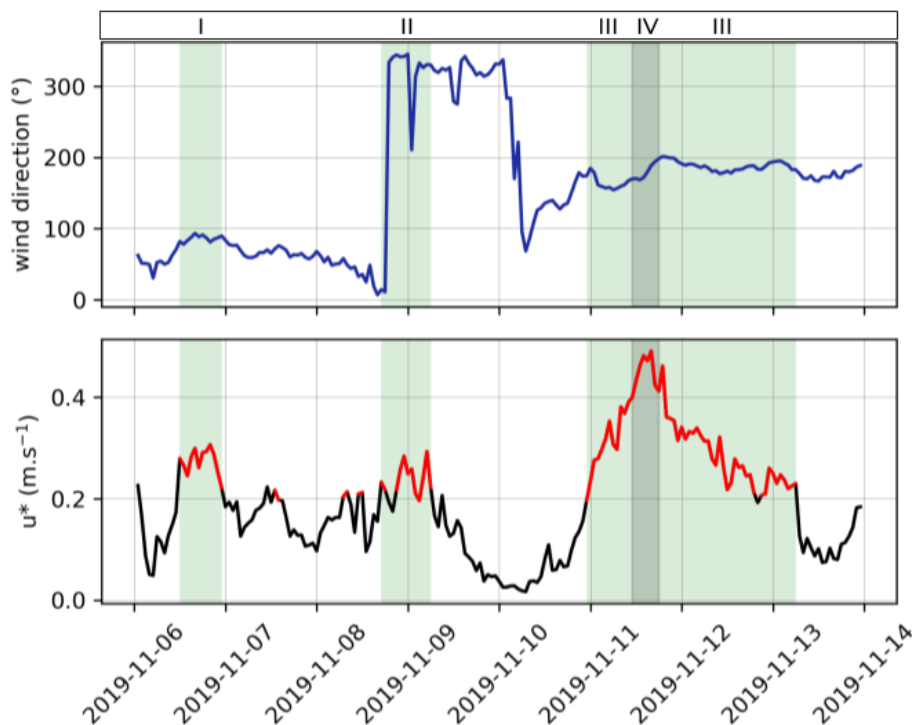
Figure 3. Time series for wind direction (top) and surface friction velocity (bottom) measured in the period between the successive TLS measurements. The values displayed are an average of measurements taken at 2 m, 6 m and 10 m height. The green-colored areas (I to III) correspond to the time periods for which snow movement was assumed to occur. The darker area (IV) shows the time span during which precipitation was measured by the radar. Source: Alfred-Wegener-Institut Helmholtz-Zentrum für Polar- und Meeresforschung (AWI) (2020) & Matthew Shupe et al. (2021).

2.4 Modelling assumptions

To reduce the computational complexity while still enabling relevant modelling, several assumptions were made. First, only
310 gravity and fluid-particle drag were considered in the force balance to solve the grain trajectories (Eq.1). As commonly done in snow transport applications (e.g. Gauer (2001)) we neglect the other small particle–fluid interaction forces commonly found in nature (e.g. buoyancy, pressure gradient) as well as the inter-particle collisional forces. Second, we adopted a parcel-based approach meaning that the particle population was represented by clouds of particles (parcels) with homogeneous properties. This technique does not take into account the clustering effect of particles represented by a single parcel (Radl and Sundaresan,
315 2013) and tends to minimize the variety in particle properties.

Turning now to Eulerian-phase modelling, the RANS method that we employed is based on ensemble-averaged governing equations and cannot predict the local unsteadiness (eddies) in the flow (e.g. Stull (1988)); the representation of the intermittent

Table 2. Particle properties employed in the sea ice OpenFOAM simulation.

Variable	Symbol	Value	Unit
Mean diameter	d_m	0.2	mm
Minimum diameter	d_{min}	0.05	mm
Maximum diameter	d_{max}	0.5	mm
Standard deviation of diameter	d_{std}	0.05	mm
Particle density (ice)	ρ_p	900	kg.m^{-3}
Snowfall rate	I	0.39	mm$_{water}$.h^{-1}
Shear stress threshold constant	A	0.2	-
Bed cohesion	ϕ	10^{-9}	J
Time of saltation initiation	t_{init}	100	s

snow transport is thus only partial, which can introduce bias in the modelled snow mass flux and ultimately in the distribution patterns.

320   Additional limitations arise from the forcing of the model. A one-week period with heterogeneous wind is represented by four discrete events only, based on a constant friction velocity threshold (Sect. 2.3.4). The onset of snow transport is in reality time- and environment-dependent and the periods with saltation may have been poorly estimated. We are aware that these restrictive representations of natural phenomena may have limited the performance of the results presented hereafter. However, they remain acceptable for a semi-quantitative comparison such as the one performed in this work.

3   Results

3.1   Snow distribution patterns per event

Figures 4 and 5 report the results, respectively, of the extrapolated areal snow-mass distribution and friction velocity produced by our OpenFOAM snow model for the four selected atmospheric events (I−IV). The wind direction is represented in each sub-figure by an arrow. For all the numerical simulations, the effect of the sea ice topography on the snow surface distribution was clearly captured; the snow particles appear to deposit on the lee-ward side of the pressure ridge whereas they get eroded on its wind-ward side and at the top. This spatial pattern agrees with previous observations suggesting that snow drift aprons mostly form in the lee of sea ice blocks and pressure ridges (Sturm et al., 2002; Massom et al., 2001). Also, it is in line with snow distribution measurements on an Antarctic sea ice floe which revealed strong deposition behind topographic obstacles according to the predominant wind direction (Trujillo et al., 2016).

Table 3. Numerical quantitative results for the OpenFOAM sea ice simulations per identified event (I-IV) between November 6 and 13, 2019. Relative areal proportion, average values and overall range for snow deposition and erosion are presented.

Event	Snow deposition			Snow erosion		
	mean kg.m^{-2}	maximum kg.m^{-2}	area %	mean kg.m^{-2}	maximum kg.m^{-2}	area %
I	0.23	12.8	48.3	-0.22	-22.0	51.2
II	0.05	5.30	52.6	-0.05	-11.3	46.9
III	0.78	60.2	50.0	-0.79	-86.9	49.3
IV	2.51	18.89	93.4	-3.91	-42.7	6.6

Increased snow deposition is found in zones of highly-turbulent, decelerated flow, which typically appear behind the topographical obstacles; such wake regions are colored in blue in the surface friction velocity plots (Fig. 5). Alternatively, a fluid that is deviated by the terrain usually accelerates which strengthens its forces on the ground and enhances snow erosion, as observed over the ridge and along steep slopes. This connection between surface friction velocity and snow-mass distribution is highlighted through the comparison of their corresponding surface patterns.

The snow distribution results (Fig. 4) as well as the average (extreme) values for snow deposition and erosion (Table 3) are variable between the simulations: factors such as the slope angle encountered by the flow, the duration of the wind events and the magnitude of the fluid forcing can explain these differences. The mean snow deposition and erosion are specifically enhanced for the event with precipitation (IV). The precipitation particles combined with strong flow seem to favour the uplift of the snow grains when hitting the surface. Figure 4-IV shows that deposition is ubiquitous over the domain (93.4% of the area) but remains stronger at the lee of the ridge. Quantitatively speaking, the extent of the areal snow-mass range indicates that event II is the least influential on the snow distribution as it represents at most 50% of the redistribution values obtained in the other cases. This most probably stems from the lower duration and friction velocity characteristic of that period. Contrastingly, simulations III and IV have largest erosion and deposition values and therefore have the most influence on the combined snow distribution results. Note that the mean snow mass changes (erosion and deposition) in simulations I-III are close to zero, revealing a balanced mass system.

3.2 Comparison to MOSAiC measurements

After evaluating the numerical results for each event individually, the left of Figure 6 displays the snow distribution patterns obtained by their combination; the right-side illustration shows the snow-mass distribution changes measured during MOSAiC over the period of interest (November 6−13).

A qualitative analysis reveals that a nearly uniform layer of deposited snow attributable to event IV has formed over the numerical domain, which contrasts with measurements where snow mass changes are close to zero in flat areas. This discrepancy put aside, the model results satisfyingly agree with the measurements on the location of enhanced snow deposition:

circles **A** to **D** in Figure 6 highlight zones of accumulated snow that appear in both the model and measurements. Yet, there are features that were not reproduced by OpenFOAM: the northern side of the ridge (above **B**) and the zone between **C** and **D** show enhanced snow accumulation, which is almost absent in the combined simulation output. The closest similarity in deposition patterns (neglecting the homogeneously higher deposition) is found with simulation IV (Fig. 4), which shows snow accumulation between **C** and **D** and more elongated patches parallel to the predominant wind direction. Thus, a strong flow together with precipitation seems to mostly account for the measured distribution. Regarding erosion, the wind-ward side and top of the ridge show snow depletion in both simulated and measured data, although to different extents. The measured erosion is more accentuated, especially in between the fragments of the ridged ice (**B**-**C**, **C**-**D**) and in the southern area of the domain . We also find that some deposition patterns revealing the micro-relief of the ice surface were modelled in the flat areas around the ridge but are not as apparent in the measurements: they emerge only in localized sections (e.g. South-East of the domain) . The relative proportion of erosion to the total area represents 9.8% and 62.7% in the model and measurements, respectively.

Quantitatively, our model appears only partially successful in predicting the snow mass changes over the numerical domain. Figure 7 shows the probability distribution of both measurements (blue) and simulation results (green). snowBedFoam 1.0. underestimates the erosion found in the measurements and yields a higher proportion of cells with moderate snow deposition (between 0 and 8 $kg.m^{-2}$). In general, the measured snow mass change has more extreme values than in the model: it has a standard deviation of 10.7 $kg.m^{-2}$ compared to 4.8 $kg.m^{-2}$ for snowBedFoam. The mean snow mass change value is positive for the combined output (2.09 $kg.m^{-2}$), due to the addition of precipitation particles in simulation IV: the periodic set-up implies that any added mass is systematically re-injected through the lateral patches of the domain and ends up depositing on its surface. Note that this mean value approximately corresponds to the mass per surface computed using the average precipitation rate and the surface area or the domain (2.73 $kg.m^{-2}$). The measurements reveal an overall slight erosion (-0.06 $kg.m^{-2}$) : the snow has been transported outside of the domain. A number of reasons may have caused these dissimilarities, which will be discussed in the next section.

4   Discussion

Figure 6 reveals that the main zones of snow deposition and depletion were captured by snowBedFoam, even though it simulates a higher snow deposition on average in the flatter area of the domain. The deposition patterns scanned during MOSAiC show some satisfying agreement with the simulations, except for a few patches of enhanced accumulation, which are missing in the numerical results. Regarding erosion, the model underestimates it in most locations, although spatial erosion is qualitatively well captured at the ridge. The locations with lower erosion appearing in Figure 4 were likely damped by the precipitation particles settling on the surface (Event IV). Larger snow mass change values are overall reached by the measurements. There may be multiple reasons for these results.

1. *Simplification of wind transport*: the snow transport by the wind may be oversimplified due to a limited representation of the real aeolian conditions. For the selected events, the ratio of the standard deviation between the measurements to the average value shows a range of 6-24% for the wind direction and 10-21% for the wind speed (one minute interval). We

used four averaged values for wind speed and direction in OpenFOAM to represent a one-week period of measurements. This implies that many specific wind conditions causing snow redistribution were not represented in the simulations, along with their associated effect on the snow patterns. The full directional variability of the wind forcing is likely not well represented by our approach. For the under-represented deposition patches between circles **C** and **D** in particular,

395 Figure 4—IV demonstrates that a stronger flow enables their reproduction by the model at the precise spots. Taking mean wind speed values for forcing tends to damp the intermittent variations of the atmospheric flow, which could have lead to this unmodeled snow accumulation which is present in the TLS data.

2. *Evolution of ice surface structures:* Besides the forcing parameters, some topography-related aspects could explain missing snow features in the model. It is expected that the aeolian redistribution of snow gradually modifies the roughness

400 and topography of the sea ice surface, leading to variations in the flow field and thus in the snow transport processes (Andreas and Claffey, 1995). The invariant mesh that we employ in our simulations neglects this temporal evolution. This could explain why the measurements do not contain the micro-scale distribution patterns found in the north of the modelled ridge: they may have been gradually flattened in reality. Also, the more elongated features of deposition found in the scans could result from the build-up of snow bedforms at the lee of the ridge, which gradually displaced the depo-

405 sition maximum downwind. Future work will explore the dynamic meshing of the sea ice surface within OpenFOAM as a solution to this modelling limitation.

3. *Atmospheric stability*: Furthermore, the non-consideration of meteorological conditions such as atmospheric stability may have an effect. Various authors have shown that atmospheric stability can have a strong influence on the development of the local near-surface flow field and the associated deposition patterns, together with topography and wind speed

410 (Wang and Huang, 2017; Gerber et al., 2017; Comola et al., 2019). Atmospheric stability influences the vertical motion of the flow, which can in turn affect the settling of snow particles. The neutrally stable flow imposed in OpenFOAM overlooks this aspect and may introduce inaccuracies in the simulated snow distribution.

4. *Dimensionless parameters - summary:* Overall, we can reasonably assume that the (limited) qualitative disparities in snow distribution between numerical and TLS data are due to a combination of causes. Recent findings of Comola et al.

415 (2019) suggest that different distribution patterns can emerge from different combinations of dimensionless parameters expressing atmospheric stability, particle inertia and length and velocity scales (Froude and Stokes numbers). The simplifications for flow, grain shape, atmospheric conditions and topography imposed by our modelling framework inevitably bring errors; taking this into consideration, the agreement appears to be very satisfying.

Besides the qualitative comparison, we observe that the quantitative performance of our snow model is not optimal. Erosion

420 is underestimated by snowBedFoam both at the ridge and in flatter areas, while deposition is underpredicted in the main snow accumulation patches. We identified sources of error in both the model and measurements that could potentially explain the mismatch.

1. *Precipitation and other measurements*: There are several limitations related to the MOSAiC measurements that could explain the quantitative disagreement with the model. First, an influential source of unreliability lies in the KAZR-derived snowfall estimates. The latter showed a tendency to overestimate precipitation during the MOSAiC campaign (Wagner et al., 2021), which may be the case for event IV. Exaggerated snowfall rates in the simulations would generate an excess of particles cancelling the erosive effect of the other simulations and leading to more "damped" snow distribution patterns in the combined output. The snowfall rate has a significant impact on the average snow deposition value obtained in the snowBedFoam simulations and should be adjusted with care. Moreover, a source of unreliability in the DEMs can originate from the positions of individual points within the scan along with the errors in elevation difference between the two successive surveys: some snow-depth changes could be subject to a measurement error. However, this is expected to be small. In addition, the snow-mass values presented in Figure 6 derive from the multiplication of height data with a constant snow density, which is in reality variable from location to location. Hence, the snow-mass results presented here have errors in representing the actual mass distribution. At last, it is probable that the wind-related measurements brought additional uncertainty in the particle and flow settings of our model; all of these errors combined are expected to have influenced the numerical results.

2. *Temporal variability of the snow cover*: In snowBedFoam, the aerodynamic entrainment of snow is modelled through a fixed threshold value which neglects the temporal changes in the environmental conditions and snowbed properties (metamorphism). The sintering of grains has been identified in the literature as a key component of the equilibrium between erosion and deposition of snow (Blackford, 2007): strong bonds between snow particles might prevent their subsequent erosion and generate stationary bedforms (Filhol and Sturm, 2015). Freshly-fallen snow particles are not bound, thus highly erodible : their transport usually occurs at lower wind speeds than for ice or compacted snow (Guala et al., 2008), resulting in higher mass flux and deposition at the lee side of the ridge. Such conditions likely correspond to the period following the precipitation event on November 11 (Fig. 3), but were not accounted for in the simulations. These observations suggest that the potential coupling to a snow modelling tool evaluating the snow transport threshold based on meteorological time series such as SNOWPACK (Lehning et al., 1999) could bring great improvement to the results of the CFD model alone.

3. *Spatial heterogeneity of sea ice surface properties:* An uniform snow cover (unvarying parameters over the domain) was considered in our numerical simulations, which contrasts with real snow layers. The latter are usually complex and under natural conditions, they exhibit irregular boundaries and a wide range of grain and bond characteristics when traced laterally (Sturm and Benson, 2004). The same observations apply to snow in the sea ice system, which complicates its modelling. Challenges are here twofold. First, it is difficult to characterize the snow cover properties over space due to a lack of data at the level of detail needed for our simulations. Second, the mathematical parametrization of the snowpack properties has not been fully established yet. Constants such as A (Bagnold's shear stress threshold constant, Eq.10) or ϕ (grain cohesion parameter, Eq.13) are a way to include the snowpack properties in snowBedFoam 1.0. but the exact connection between their value and the grain characteristics is still unclear. We are aware that the restricted inclusion

of the spatial variability in snow properties may have lowered the accuracy of our results; however, further research is
needed to investigate the parametrization of the snow surface properties, which will not be addressed in the present work.

4. *Turbulence scheme:* Furthermore, the use of RANS as a turbulence scheme implies the modelling of averaged flow-
fields only, which simplifies the fluctuating nature of snow transport and likely introduces a bias (Groot Zwaaftink
et al., 2013). Turbulent eddies intermittently enhance snow erosion and deposition; such atmospheric structures could
have incrementally produced sheltered stationary bedforms in the lee of the ridge and lead to the higher accumulation
measured by TLS.

5. *Periodic boundary conditions:* At last, the periodic boundary condition imposed at the lateral edges of the domain
treats them as if they were physically connected (OpenCFD Ltd, 2019). This approach is usually employed for repeated
geometries that only partially apply to sea ice. Figure 1 shows that a relatively flat area precedes the gridded ridge in
reality, according to the predominant wind direction (south). The absence of aerodynamic obstacles in the actual terrain
could potentially lead to a higher snow transport flux than in OpenFOAM where the PBCs imply the artificial repetition
of the simulated topography on all sides of the numerical domain. In other words, the accumulation of snow particles in
reality may occur over vaster areas than in the model where we artificially create successive deposition over the ridges.
The higher snow erosion and subsequent deposition observed in the scans could come from larger-scale variations in the
horizontal mass flux. In addition, PBCs imply that the eroded particles necessarily deposit somewhere in the numerical
domain as they are constantly re-injected through the connected patches. The same applies to injected (precipitation)
particles: this explains why there is an important amount of cells (90% of the surface) with a positive snow mass change
in the model (Figure 7). Comparing snow measurements on sea ice to a numerical model, which is conservative in terms
of mass, highlights the effect of wind redistribution in this environment and can help to understand the snow mass fluxes
going in and out of the real system. snowBedFoam 1.0. appears here as an useful tool to assess the snow mass loss (gain)
on a given piece of sea ice and to identify potential snow mass sinks (sources). For example, Déry and Tremblay (2004)
showed that the total amount of blowing snow loss into the Arctic Ocean may reach between 60 - 100 % but difficulties
are encountered in measuring such values; numerical models can help refine these quantitative estimates when comparing
their mass-conservative results to real snow distribution measurements.

The limitations identified here highlight the current challenges encountered in the modelling of snow deposition over com-
plex terrain. The spatial variability of the snow cover is caused by physical processes acting at different spatial scales (Mott
et al., 2014) and the contribution of each is hardly distinguishable in the field measurements (Gerber et al., 2017). Thus, this
field of research relies to a great extent on mathematical modelling (Comola et al., 2019), which inevitably simplifies the com-
plex snow-wind interaction due to both numerical and computational constraints. In the case of sea ice, the inhomogeneous
snow distribution mostly results from the wind and precipitation interacting with the snow surface, similarly to what is ob-
served in alpine terrain (Mott and Lehning, 2010). Our snowBedFoam 1.0. model offers the potential to separately simulate the
preferential deposition of precipitation (Lehning et al., 2008) and the transport of previously deposited snow, as observable in

490   Figure 4. Thus, the role played by each in the spatial variability of snow deposition can be singled out to better understand its underlying mechanisms.

5   Conclusions

In this study we introduce snowBedFoam 1.0., a snow transport model developed on the basis of the standard Lagrangian particle tracking library of the computational fluid dynamics (CFD) software OpenFOAM. We applied it to simulate the snow

495   accumulation patterns on Arctic sea ice using terrestrial laser scan observations from MOSAiC. To our knowledge this is the first publication on a Eulerian-Lagrangian snow deposition model combined with sea ice topographical data from lidar measurements. Qualitatively, results show that most of the snow distribution patterns were accurately captured by the numerical simulations; from a quantitative point of view, however, the erosion and enhanced deposition were under-represented by the model while an ubiquitous snow deposition was simulated. This limited quantitative performance is attributed to various

500   sources such as the CFD numerics, the oversimplification of the real conditions in the model (wind, snowpack properties) or to the measurements themselves. Further improvements should be incorporated into our modelling approach, notably by coupling snowBedFoam to snowpack models or by including other factors influencing snow transport such as the atmospheric stability. The manifold snow - wind interactions ask for very complex modelling, which is computationally expensive and remains challenging despite the recent developments in computer science.

505   Although performance was not perfect, our model development presents a significant step towards the accurate modelling of snow deposition on sea ice. This tool could further be used in the assessment of snow mass balance components to improve precipitation estimates through measurements. Overall, considerable progress has been made towards the small-scale study of snow distribution as the model may be further applied to other topographies, with the advantage of incorporating elevation data stemming from laser scans.

510   *Code and data availability.* The scripts of the snowBedFoam 1.0. model are available on the EnviDat data repository of the Swiss Federal Institute WSL (Hames et al., 2021) along with the preliminary wind tower data for the specific period of the simulations. The latter are part of a larger dataset which will be published in the near future by M.D.S. and his team. The Terrestrial Laser Scan data processed by D.C.-S. can be found on the Arctic Data Center repository (Clemens-Sewall, 2021).

Author contributions. O.H. took the lead in writing the manuscript but declares joint first-authorship with M.J. Both M.J. and O.H. imple-

515   mented the snow transport model in OpenFOAM and ran the snowBedFoam 1.0. simulations. D. C.-S. and C. P. were responsible for the planning of the TLS campaign and provided the scanner and accessories. D. C.-S. processed the TLS point clouds to generate the sea ice surface position data. I. R. and D. N. W. conducted the scans and D. N. W. measured and processed snow density, TLS and KAZR data. He and M.S. were in charge of the planning and coordination with the MOSAiC organization. M.D.S. and his team measured and processed the meteorological data employed for the model forcing, which we published in its preliminary version. M.D.S. was also the principal inves-

tigator for the ARM involvement in MOSAiC (KAZR data). M.L. encouraged O.H. and M.J. to investigate the snow transport on sea ice, gave regular input on the implementation of physical processes and supervised the work. Besides, he helped design together with M.S. the numerical set-up and relevant MOSAIC field deployments.

Competing interests. The authors declare that they have no conflict of interest.

Acknowledgements. The authors thank Varun Sharma and Daniela Brito Melo for their help in better understanding their Large Eddy Simulation-Lagrangian Particle Tracking FORTRAN code as well as sharing their knowledge about fluid dynamics. Are also thanked Franziska Gerber and Robert Kenner for their valuable help and guidance in the processing of the TLS data. Finally, the authors thank all MOSAiC participants for contributing to the paper in one way or another: the MOSAiC logistics- and data team, the ship's personnel, members from all science teams on board, the ARM crew, the MOSAiC project team and the project board.

The data used in this manuscript was produced as part of the international Multidisciplinary drifting Observatory for the Study of the Arctic Climate (MOSAiC) with the tag MOSAiC20192020 and the Polarstern expedition number AWI_PS122_00. Precipitation data were obtained from the Atmospheric Radiation Measurement (ARM) user facility, a U.S. Department of Energy (DOE) Office of Science user facility managed by the Biological and Environmental Research Program. M.D.S. was supported by the DOE Atmospheric System Research Program (DE-SC0019251, DE-SC0021341).

This project is co-supported by the Swiss National Science Foundation-SNF, grant number 200021E-160667 and 200020-179130.

References

Ackley, S. F., Lange, M. A., and Wadhams, P.: Snow cover effects on Antarctic sea ice thickness, in: Sea ice properties and processes: Proc of the W F Weeks Sea Ice Symposium (S F Ackley, W F Weeks, eds) CRREL monograph 90-1, pp. 16–21, 1990.

Alfred-Wegener-Institut Helmholtz-Zentrum für Polar- und Meeresforschung (AWI): Polar Research and Supply Vessel POLARSTERN Operated by the Alfred-Wegener-Institute, Journal of large-scale research facilities, 3, A119, https://doi.org/http://dx.doi.org/10.17815/jlsrf-3-163, 2017.

Alfred-Wegener-Institut Helmholtz-Zentrum für Polar- und Meeresforschung (AWI): The MOSAiC expedition, https://mosaic-expedition.org/, 2020.

Anderson, R. S. and Haff, P. K.: Wind modification and bed response during saltation of sand in air, pp. 21–51, Springer Vienna, 1991.

Andreas, E. L. and Claffey, K. J.: Air-ice drag coefficients in the western Weddell Sea: 1. Values deduced from profile measurements, Journal of Geophysical Research: Oceans, 100, 4821–4831, https://doi.org/10.1029/94JC02015, 1995.

Atmospheric Radiation Measurement (ARM) user facility: Ka ARM Zenith Radar (KAZRCFRGE). 2019-10-11 to 2020-09-20, ARM Mobile Facility (MOS) MOSAIC (Drifting Obs - Study of Arctic Climate); AMF2 (M1)., http://dx.doi.org/10.5439/1498936, compiled by I. Lindenmaier, D. Nelson, B. Isom, J. Hardin, A. Matthews, T. Wendler and V. Castro, 2019.

Bagnold, R.: The Physics of Blown Sand and Desert Dune, pp. 77–84, https://doi.org/10.1007/978-94-009-5682-7_6, 1941.

Bintanja, R., van der Wiel, K., van der Linden, E. C., Reusen, J., Bogerd, L., Krikken, F., and Selten, F. M.: Strong future increases in Arctic precipitation variability linked to poleward moisture transport, Science Advances, 6, https://doi.org/10.1126/sciadv.aax6869, 2020.

Blackford, J. R.: Sintering and microstructure of ice: a review, Journal of Physics D: Applied Physics, 40, R355–R385, https://doi.org/10.1088/0022-3727/40/21/r02, 2007.

Boisvert, L. N., Webster, M. A., Petty, A. A., Markus, T., Bromwich, D. H., and Cullather, R. I.: Intercomparison of Precipitation Estimates over the Arctic Ocean and Its Peripheral Seas from Reanalyses, Journal of Climate, 31, 8441–8462, https://doi.org/10.1175/JCLI-D-18-0125.1, 2018.

Cleary, P. and Prakash, M.: Discrete-element modelling and smoothed particle hydrodynamics: Potential in the environmental sciences, Philosophical transactions. Series A, Mathematical, physical, and engineering sciences, 362, 2003–30, https://doi.org/10.1098/rsta.2004.1428, 2004.

Clemens-Sewall, D.: Terrestrial Laser Scans of the Snow 2 area of the Multidisciplinary drifting Observatory for the Study of Arctic Climate from November 6 and 13 2019, Arctic Data Center, https://doi.org/10.18739/A2DZ03304, 2021.

Clifton, A. and Lehning, M.: Improvement and validation of a snow saltation model using wind tunnel measurements, Earth Surface Processes and Landforms, 33, 2156–2173, https://doi.org/10.1002/esp.1673, 2008.

Clifton, A., Rüedi, J.-D., and Lehning, M.: Snow saltation threshold measurements in a drifting-snow wind tunnel, Journal of Glaciology, 52, 585–596, https://doi.org/10.3189/172756506781828430, 2006.

Comola, F. and Lehning, M.: Energy and momentum conserving model of splash entrainment in sand and snow saltation: SPLASH ENTRAINMENT OF SAND AND SNOW, Geophysical Research Letters, https://doi.org/10.1002/2016GL071822, 2017.

Comola, F., Giometto, M. G., Salesky, S. T., Parlange, M. B., and Lehning, M.: Preferential Deposition of Snow and Dust Over Hills: Governing Processes and Relevant Scales, Journal of Geophysical Research: Atmospheres, 124, 7951–7974, https://doi.org/10.1029/2018JD029614, 2019.

Doorschot, J. and Lehning, M.: Equilibrium Saltation: Mass Fluxes, Aerodynamic Entrainment, and Dependence on Grain Properties, Boundary-Layer Meteorology, 104, 111–130, 2002.

Doorschot, J., Lehning, M., and Vrouwe, A.: Field measurements of snow-drift threshold and mass fluxes, and related model simulations, Boundary-Layer Meteorology, 113, 347–368, https://doi.org/10.1007/s10546-004-8659-z, 2004.

575 Déry, S. and Tremblay, B.: Modeling the Effects of Wind Redistribution on the Snow Mass Budget of Polar Sea Ice, Journal of Physical Oceanography - J PHYS OCEANOGR, 34, https://doi.org/10.1175/1520-0485(2004)034<0258:MTEOWR>2.0.CO;2, 2004.

Fernandes, C., Semyonov, D., Ferrás, L., and Nobrega, J.: Validation of the CFD-DPM solver DPMFoam in OpenFOAM® through analytical, numerical and experimental comparisons, Granular Matter, 20, https://doi.org/10.1007/s10035-018-0834-x, 2018.

Filhol, S. and Sturm, M.: Snow bedforms: A review, new data, and a formation model, Journal of Geophysical Research: Earth Surface, 120,
580 https://doi.org/10.1002/2015JF003529, 2015.

Gauer, P.: Numerical modeling of blowing and drifting snow in Alpine terrain, Journal of Glaciology, 47, 97–110, https://doi.org/10.3189/172756501781832476, 2001.

Gerber, F., Lehning, M., Hoch, S. W., and Mott, R.: A close-ridge small-scale atmospheric flow field and its influence on snow accumulation, Journal of Geophysical Research: Atmospheres, 122, 7737–7754, https://doi.org/10.1002/2016JD026258, 2017.

585 Gromke, C. C., Horender, S., Walter, B., and Lehning, M.: Snow particle characteristics in the saltation layer, Journal of Glaciology, 60, 431–439, 2014.

Groot Zwaaftink, C., Mott, R., and Lehning, M.: Seasonal simulation of drifting snow sublimation in Alpine terrain, Water Resources Research, 49, 1581–1590, https://doi.org/10.1002/wrcr.20137, 2013.

Grünewald, T., Schirmer, M., Mott, R., and Lehning, M.: Spatial and temporal variability of snow depth and SWE in a small mountain
590 catchment, The Cryosphere Discussions, 4, https://doi.org/10.5194/tcd-4-1-2010, 2010.

Guala, M., Manes, C., Clifton, A., and Lehning, M.: On the saltation of fresh snow in a wind tunnel: Profile characterization and single particle statistics, Journal of Geophysical Research: Earth Surface, 113, https://doi.org/https://doi.org/10.1029/2007JF000975, 2008.

Hames, O., Jafari, M., and Lehning, M.: snowBedFoam: an OpenFOAM Eulerian-Lagrangian solver for modelling snow transport, https://doi.org/http://dx.doi.org/10.16904/envidat.223, 2021.

595 He, S. and Ohara, N.: A New Formula for Estimating the Threshold Wind Speed for Snow Movement, Journal of Advances in Modeling Earth Systems, 9, 2514–2525, 2017.

Huntington, H., Gearheard, S., Holm, L., Noongwook, G., Opie, M., and Sanguya, J.: Sea ice is our beautiful garden: Indigenous perspectives on sea ice in the Arctic, pp. 583–599, https://doi.org/10.1002/9781118778371.ch25, 2016.

Kok, J. and Rennó, N.: A comprehensive numerical model of steady state saltation (COMSALT), Journal of Geophysical Research (Atmo-
600 spheres), 114, 17 204–, https://doi.org/10.1029/2009JD011702, 2009.

Launder, B. and Spalding, D.: The numerical computation of turbulent flows, Comput. Methods Appl. Mech. Eng., 103, 456–460, 1974.

Lehning, M., Bartelt, P., Brown, B., Russi, T., Stöckli, U., and Zimmerli, M.: SNOWPACK model calculations for avalanche warning based upon a network of weather and snow stations, Cold Regions Science and Technology, 30, 145–157, https://doi.org/10.1016/S0165-232X(99)00022-1, 1999.

605 Lehning, M., Löwe, H., Ryser, M., and Raderschall, N.: Inhomogeneous precipitation distribution and snow transport in steep terrain, Water Resour. Res, 44, https://doi.org/10.1029/2007WR006545, 2008.

Leonard, K. and Maksym, T.: The importance of wind-blown snow redistribution to snow accumulation on Bellingshausen Sea ice, Annals of Glaciology, 52, 271–278, https://doi.org/10.3189/172756411795931651, 2011.

Liston, G., Polashenski, C., Rösel, A., Itkin, P., King, J., Merkouriadi, I., and Haapala, J.: A Distributed Snow Evolution Model for Sea Ice

610   Applications (SnowModel), Journal of Geophysical Research: Oceans, https://doi.org/10.1002/2017JC013706, 2018.

Liston, G. E. and Elder, K.: A Distributed Snow-Evolution Modeling System (SnowModel), Journal of Hydrometeorology, 7, 1259–1276, https://doi.org/10.1175/JHM548.1, 2006.

Liston, G. E., Haehnel, R. B., Sturm, M., Hiemstra, C. A., Berezovskaya, S., and Tabler, R. D.: Simulating complex snow distributions in windy environments using SnowTran-3D, Journal of Glaciology, 53, 241–256, https://doi.org/10.3189/172756507782202865, 2007.

615   Maslanik, J. A., Fowler, C., Stroeve, J., Drobot, S., Zwally, J., Yi, D., and Emery, W.: A younger, thinner Arctic ice cover: Increased potential for rapid, extensive sea-ice loss, Geophysical Research Letters, 34, https://doi.org/10.1029/2007GL032043, 2007.

Massom, R. A., Eicken, H., Hass, C., Jeffries, M. O., Drinkwater, M. R., Sturm, M., Worby, A. P., Wu, X., Lytle, V. I., Ushio, S., Morris, K., Reid, P. A., Warren, S. G., and Allison, I.: Snow on Antarctic sea ice, Reviews of Geophysics, 39, 413–445, https://doi.org/10.1029/2000RG000085, 2001.

620   Matrosov, S.: Modeling Backscatter Properties of Snowfall at Millimeter Wavelengths, Journal of The Atmospheric Sciences - J ATMOS SCI, 64, https://doi.org/10.1175/JAS3904.1, 2007.

Matthews, S., Johannessen, O., and Michelsen, L.-H.: The Geopolitical Implications Of Arctic Sea Ice Melt, The Norwegian Climate Foundation and Nansen Scientific Society, Report 02/2019, https://doi.org/10.13140/RG.2.2.13641.49765, 2019.

Mott, R. and Lehning, M.: Meteorological Modeling of Very High-Resolution Wind Fields and Snow Deposition for Mountains, Journal of

625   Hydrometeorology - J HYDROMETEOROL, 11, 934–949, https://doi.org/10.1175/2010JHM1216.1, 2010.

Mott, R., Scipión, D., Schneebeli, M., Dawes, N., Berne, A., and Lehning, M.: Orographic effects on snow deposition patterns in mountainous terrain, Journal of Geophysical Research: Atmospheres, 119, 1419–1439, https://doi.org/https://doi.org/10.1002/2013JD019880, 2014.

Moukalled, F., Mangani, L., and Darwish, M.: The Finite Volume Method in Computational Fluid Dynamics: An Advanced Introduction with OpenFOAM and Matlab, Springer Publishing Company, Incorporated, 1st edn., 2015.

630   Nemoto, M. and Nishimura, K.: Numerical simulation of snow saltation and suspension in a turbulent boundary layer, Journal of Geophysical Research: Atmospheres, 109, https://doi.org/10.1029/2004JD004657, 2004.

OpenCFD Ltd: OpenFOAM: The Open Source CFD Toolbox User Guide, https://www.openfoam.com/documentation/user-guide, 2018.

OpenCFD Ltd: OpenFOAM: The Open Source CFD Toolbox, https://www.openfoam.com, 2019.

OpenFOAM API Guide: DPMFoam.C File Reference, https://www.openfoam.com/documentation/guides/latest/api/DPMFoam_8C.html,

635   2006a.

OpenFOAM API Guide: Forces, https://www.openfoam.com/documentation/guides/latest/api/group_ _grpLagrangianIntermediateForceSubModels.html, 2006b.

OpenFOAM API Guide: SphereDragForce< CloudType > Class Template Reference, https://www.openfoam.com/documentation/guides/ latest/api/group__grpLagrangianIntermediateForceSubModels.html, 2006c.

640   Perovich, D., Meier, W., Tschudi, M., Hendricks, S., Petty, A., Divine, D., Farrell, S., Gerland, S., Haas, C., Kaleschke, L., Pavlova, O., Ricker, R., Tian-Kunze, X., Webster, M., and Wood, K.: Sea Ice, NOAA Arctic Report Card 2020, R. L. Thoman, J. Richter-Menge, and M. L. Druckenmiller, Eds., https://doi./DOI: 10.25923/n170-9h57, 2020.

Polashenski, C., Perovich, D., and Courville, Z.: The mechanisms of sea ice melt pond formation and evolution, Journal of Geophysical Research: Oceans, 117, https://doi.org/https://doi.org/10.1029/2011JC007231, 2012.

Prokop, A., Schirmer, M., Rub, M., Lehning, M., and Stocker, M.: A comparison of measurement methods: terrestrial laser scanning, tachymetry and snow probing for the determination of the spatial snow-depth distribution on slopes, Annals of Glaciology, 49, 210–216, https://doi.org/10.3189/172756408787814726, 2008.

Provost, C., Sennéchael, N., Miguet, J., Itkin, P., Rösel, A., Koenig, Z., Villacieros-Robineau, N., and Granskog, M. A.: Observations of flooding and snow-ice formation in a thinner Arctic sea-ice regime during the N-ICE2015 campaign: Influence of basal ice melt and storms, Journal of Geophysical Research: Oceans, 122, 7115–7134, https://doi.org/https://doi.org/10.1002/2016JC012011, 2017.

QGIS: QGIS Geographic Information System. Open Source Geospatial Foundation Project., http://qgis.org, 2020.

Radl, S. and Sundaresan, S.: Coarse-Grid Simulations Using Parcels: An Advanced Drag Model based on Filtered CFD-DEM Data, 2013.

RIEGL: Data Sheet: 3D Terrestrial Laser Scanner with Online Waveform Processing RIEGL VZ - 1000, RIEGL Laser Measurement Systems, http://www.riegl.com/uploads/tx_pxprieqldownloads/DataSheet_VZ-1000_2017-06-14.pdf, 2017.

RIEGL: Data Sheet: Operating and Processing software RiSCAN PRO for RIEGL 3D Laser Scanners, RIEGL Laser Measurement Systems, http://www.riegl.com/uploads/tx_pxprieqldownloads/RiSCAN-PRO_DataSheet_2020-10-07.pdf, 2020.

Sharma, V., Comola, F., and Lehning, M.: On the suitability of the Thorpe–Mason model for calculating sublimation of saltating snow, The Cryosphere, 12, 3499–3509, https://doi.org/10.5194/tc-12-3499-2018, 2018.

Sommer, C., Wever, N., Fierz, C., and Lehning, M.: Investigation of a wind-packing event in Queen Maud Land, Antarctica, The Cryosphere, 12, 2923–2939, https://doi.org/10.5194/tc-12-2923-2018, 2018.

Stull, R. B.: An Introduction to Boundary Layer Meteorology, 1988.

Sturm, M. and Benson, C.: Scales of spatial heterogeneity for perennial and seasonal snow layers, Annals of Glaciology, 38, 253–260, https://doi.org/10.3189/172756404781815112, 2004.

Sturm, M. and Massom, R. A.: Snow in the sea ice system: friend or foe?, chap. 3, pp. 65–109, John Wiley & Sons, Ltd, https://doi.org/10.1002/9781118778371.ch3, 2016.

Sturm, M., Holmgren, J., and Perovich, D.: The winter snow cover on the sea ice of the Arctic Ocean at SHEBA: Temporal evolution and spatial variability, J. Geophys. Res, 107, 2002.

Trujillo, E., Leonard, K., Maksym, T., and Lehning, M.: Changes in Snow Distribution and Surface Topography Following a Snowstorm on Antarctic Sea Ice, Journal of Geophysical Research: Earth Surface, 121, https://doi.org/10.1002/2016JF003893, 2016.

Wagner, D. N., Shupe, M. D., Persson, O. G., Uttal, T., Frey, M. M., Kirchgaessner, A., Schneebeli, M., Jaggi, M., Macfarlane, A. R., Itkin, P., Arndt, S., Hendricks, S., Krampe, D., Ricker, R., Regnery, J., Kolabutin, N., Shimanshuck, E., Oggier, M., Raphael, I., and Lehning, M.: Snowfall and snow accumulation processes during the MOSAiC winter and spring season, The Cryosphere Discussions, 2021, 1–48, https://doi.org/10.5194/tc-2021-126, 2021.

Wang, Z. and Huang, N.: Numerical simulation of the falling snow deposition over complex terrain, Journal of Geophysical Research: Atmospheres, 122, 980–1000, https://doi.org/10.1002/2016JD025316, 2017.

Webster, M., Gerland, S., Holland, M., Hunke, E., Kwok, R., Lecomte, O., Massom, R., Perovich, D., and Sturm, M.: Snow in the changing sea-ice systems, Nature Climate Change, 8, https://doi.org/10.1038/s41558-018-0286-7, 2018.

Weller, H., Tabor, G., Jasak, H., and Fureby, C.: A Tensorial Approach to Computational Continuum Mechanics Using Object Orientated Techniques, Computers in Physics, 12, 620–631, https://doi.org/10.1063/1.168744, 1998.

Yumashev, D., Hussen, K., Gille, J., and Whiteman, G.: Towards a balanced view of Arctic shipping: estimating economic impacts of emissions from increased traffic on the Northern Sea Route, Climatic Change, 143, 1–13, https://doi.org/10.1007/s10584-017-1980-6, 2017.
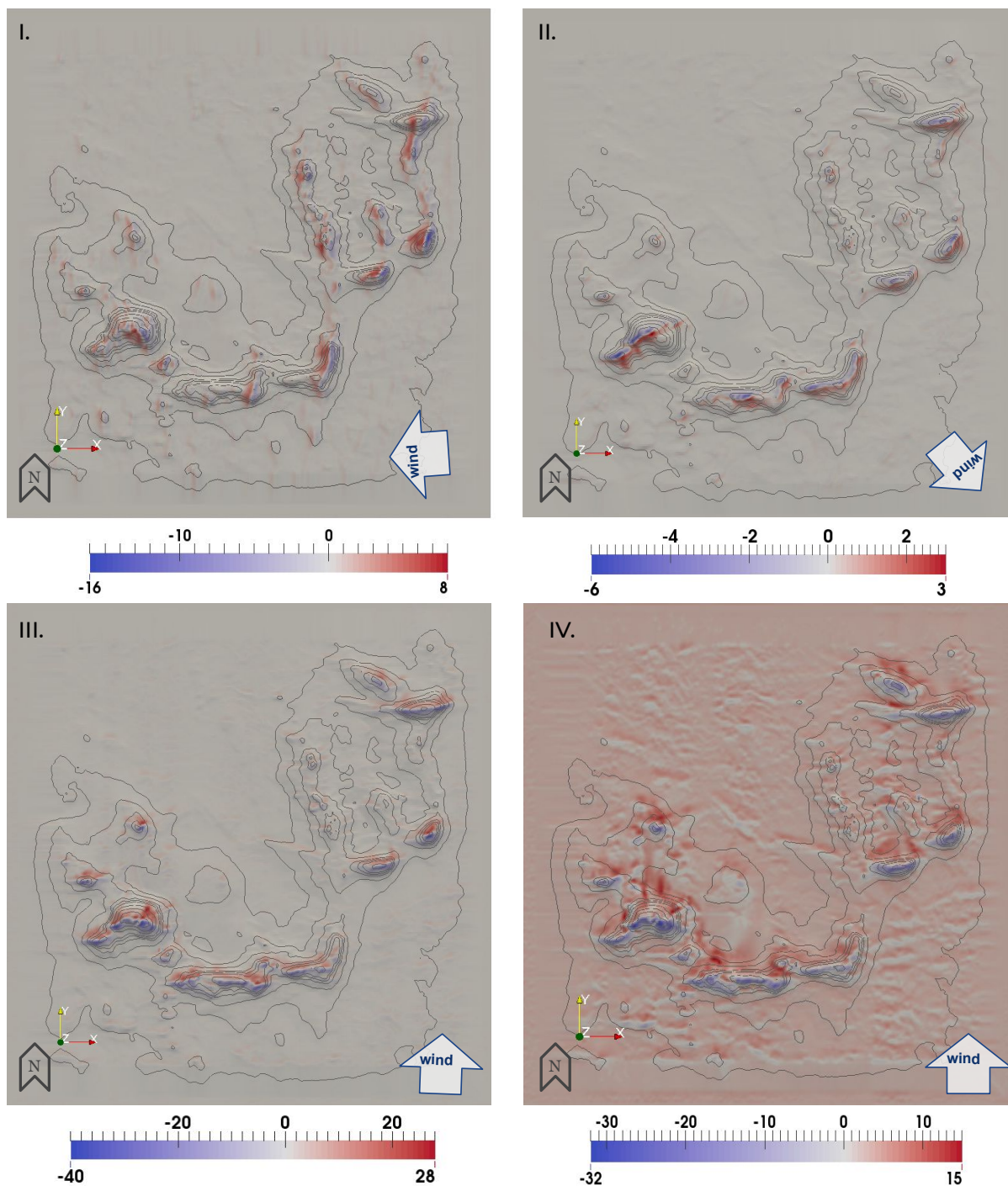
Figure 4. Extrapolated snow deposition results (kg.m^{-2}) for the four atmospheric events (I−IV) identified in the period between the two successive laser scans. The arrows in the bottom right corner indicate the direction of the fluid forcing.
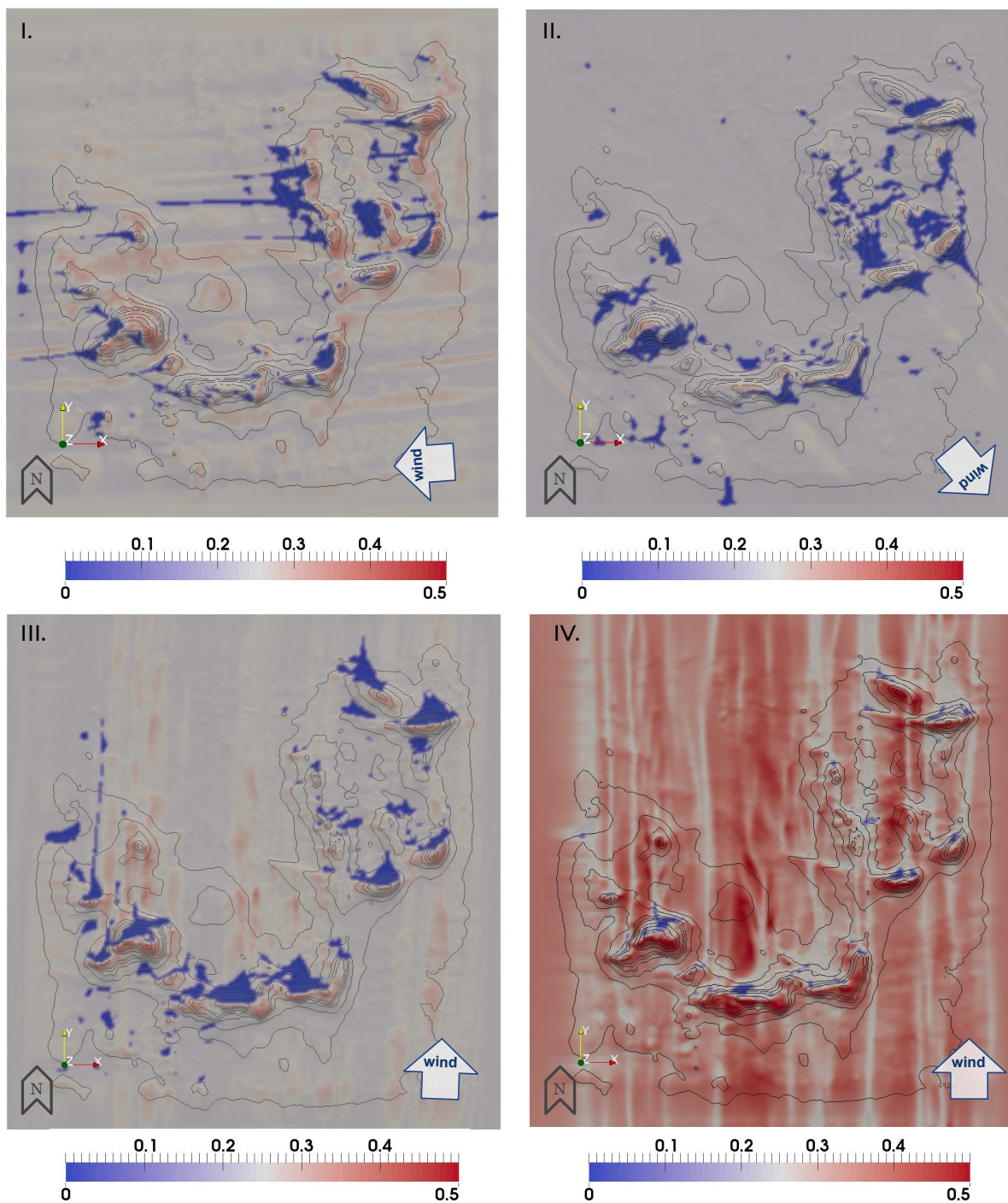
Figure 5. Friction velocity results (m.s^{-1}) for the four atmospheric events (I–IV) identified in the period between the two successive laser scans. The arrows in the bottom right corner indicate the direction of the fluid forcing.
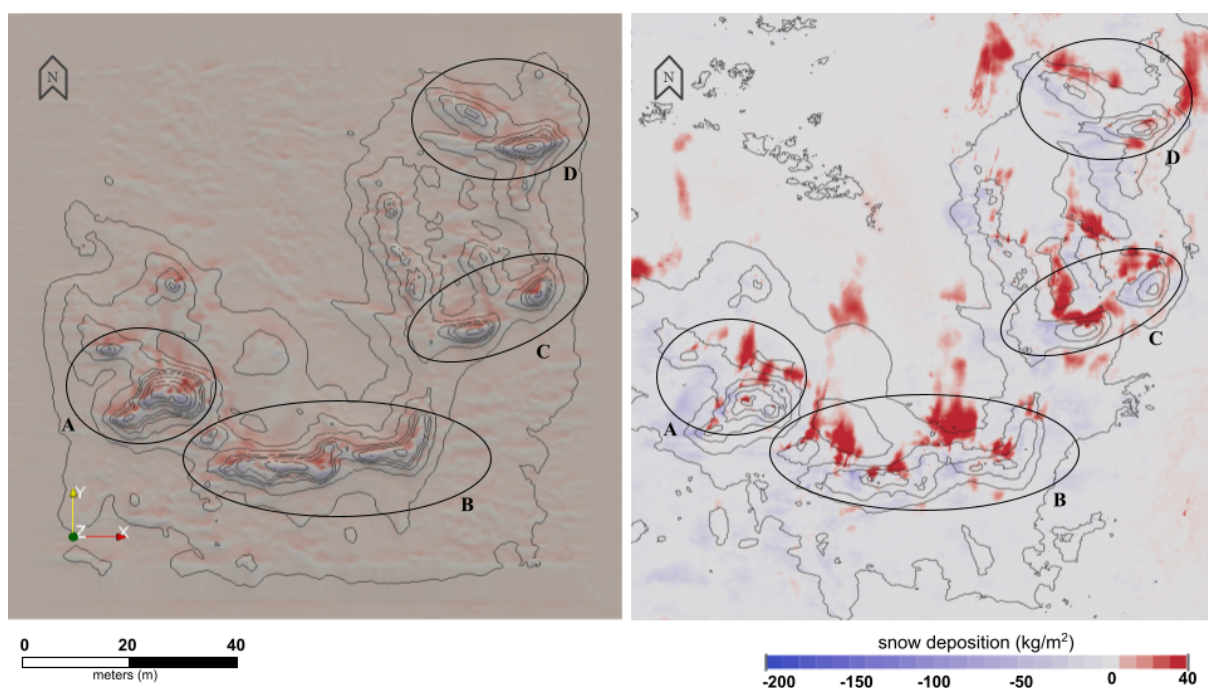
Figure 6. Left: numerical snow deposition patterns (kg.m^{-2}) after the combination of the extrapolated snowBedFoam 1.0. simulation results from the four individual atmospheric events (I−IV). **Right:** snow-mass differences obtained by differencing two successive elevation models measured during MOSAiC (Alfred-Wegener-Institut Helmholtz-Zentrum für Polar- und Meeresforschung (AWI), 2020).
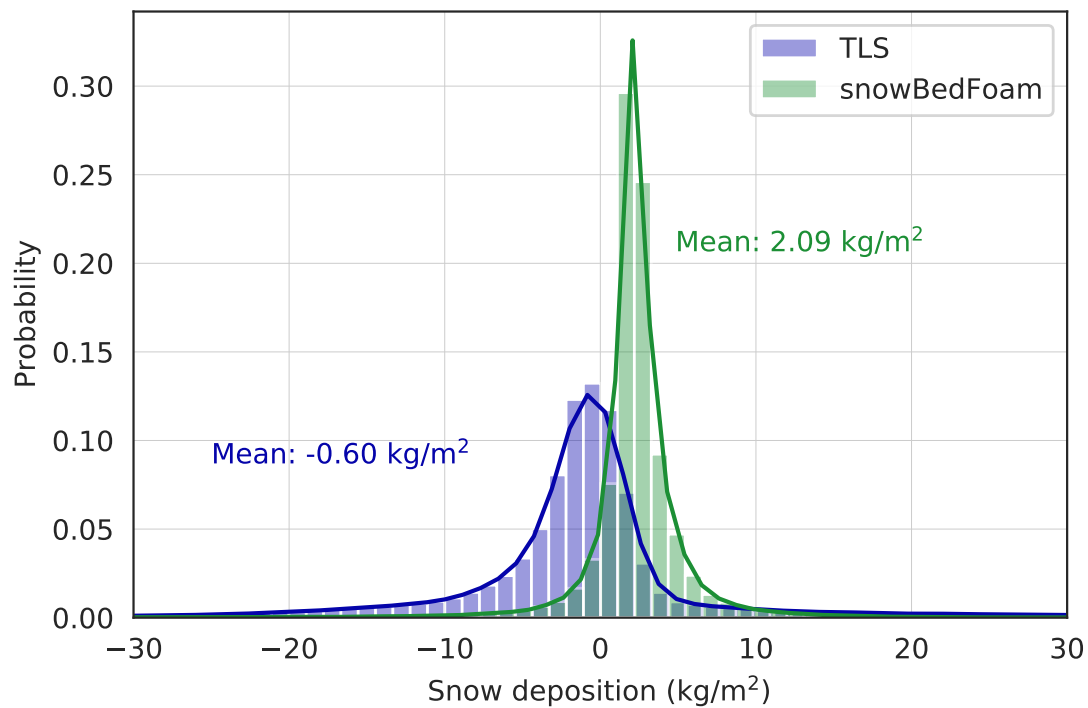
Figure 7. a. Statistical distribution of snow deposition (kg.m^{-2}) for the combined extrapolated snowBedFoam 1.0. simulation results (green) and the terrestrial laser scan measurements (blue). The average snow mass change values for TLS and OpenFOAM are displayed in the corresponding colours.